激光与光电子学进展

Actively Reconfigurable Valley Topological Edge and Corner States in Photonic Crystals Based on Phase Change Material $Ge_2Sb_2Te_5$

Li Wei[1†], Peng Yuxiang[1†], Su Peihao[1], Li Jianbo[1], Wang Kaijun[1], Liu Exian[1], Liu Jianqiang[2], He Mengdong[1*]

[1]*College of Science, Hunan Province Key Laboratory of Materials Surface & Interface Science and Technology, Central South University of Forestry and Technology, Changsha* 410004, *Hunan, China*;

[2]*College of Science, Jiujiang University, Jiujiang* 332005, *Jiangxi, China*

Abstract The immunity of topological states against backscattering and structural defects provides them with a unique advantage in the exploration and design of high-precision low-loss optical devices. However, the operating bandwidth of the topological states in certain photonic structures is difficult to actively tune and flexibly reconfigure. In this study, we propose a valley topological photonic crystal (TPC) comprising two inverse honeycomb photonic crystals, consisting of hexagonal silicon and $Ge_2Sb_2Te_5$ (GST) rods. When GST transitions from the amorphous phase to the crystalline phase, the edge band of the TPC appears as a significant redshift and is inversed from a "∪" to an "∩" shape with topological phase transition, which enables active tuning of the operating bandwidth and propagation direction of topological edge states. Both the topological edge and corner states in a triangular structure constructed using TPCs can be simultaneously adjusted and reconfigured via GST phase transition, along with a change in the group number of corner states. Using the adjustability of topological edge states and electromagnetic coupling between two different topological bearded interfaces, we develop a multichannel optical router with a high tuning degree of freedom, where channels can be actively reconfigured and their on/off states can be freely switched. Our study provides a strategy for the active regulation of topological states and may be beneficial for the development of reconfigurable topological optical devices.

Key words topological edge states; topological corner states; phase change material; active reconfiguration; topological photonic crystal

中图分类号 O436 **文献标志码** A **DOI**: 10.3788/LOP232334

1 Introduction

The discovery and application of photonic topological edge states (TESs) provide a new understanding of electromagnetic propagation and scattering. Because of the characteristics of robust edge transport, which include bypassing disorders and defects (which may appear during fabrication) and unidirectional coupling [1], TESs have become a hot topic in recent years. Researches show that TESs provide a novel platform for improving the robustness of integrated nanophotonic devices and have good potential in the application of on-chip light signal processing[2]. According to the bulk-edge correspondence principle[3], TESs are generated at the interface between two materials with different topological phases. Early approaches to realize TESs require an external magnetic field to break time-reversal (TR) symmetry[4-5]. Nevertheless, such approaches are difficult to promote and apply in practice because of the lack of materials with a strong magnetic response in the visible band and the inconvenience associated with the use of strong magnets in the microwave band [6]. Breaking TR symmetry by dynamically modifying system parameters is an alternative approach to implement TESs [7-8]. However, this approach is very complicated with significant difficulties in nanofabrication and on-chip integration. Nevertheless, the topological order of photons can also be achieved in TR-preserved systems via the quantum spin Hall effect [9-10] or valley Hall effect (VHE) [11-12], which are constructed with

收稿日期: 2023-10-20; **修回日期**: 2023-10-21; **录用日期**: 2023-11-10; **网络首发日期**: 2023-11-17

通信作者: *mengdonghe@csuft.edu.cn

† 共同第一作者

common dielectric materials and do not require magnetic components or temporal modulation. Recently, a new class of topological insulators called higher-order topological insulators that support lower-dimensional topological states have been discovered [13-16]. In a two-dimensional (2D) system, a second-order topological insulator hosts one-dimensional (1D) gapped TESs and zero-dimensional (0D) topological corner states (TCSs), and TCSs protected by bulk band topology are localized at the corners of the topological structure. TCSs can be considered a new degree of freedom (DOF) for manipulating electromagnetic waves, which offers great benefits for the development of new topological optical devices[17]. The realization of topological states is typically based on the typical periodic photonic crystal (PC) structure [18-19], and topological PCs (TPCs) with TESs and TCSs are piquing new research interest in high-Q resonators [20], topological cavities [21], corner lasers [22], high-speed waveguides [23], delay lines [11], and other related fields.

Although photonic TESs and TCSs have been successfully implemented in many topological structures and nanophotonic devices, their operation frequencies and transmission properties are difficult to manipulate for certain photonic structures, limiting their applications in topological optical devices with specific bandwidth requirements. Various approaches to facilitate the active control of topological states have been proposed. Tunable topological states can be realized in structures made of silicon or phase change materials via external stimuli (light [23], heat [24], electricity [25-26], magnetic field [27], etc.). TESs in a THz topological switch can be dynamically turned on/off by an external continuous-wave laser [28]. Changing the voltage applied to liquid crystals can result in a shift in the spectral position of topological states [29-30]. Compared with topological states with a fixed bandwidth, tunable topological states enable optical devices with high flexibility and reconfigurability. They can be optimized according to the application needs, which improve the performance and reliability of devices. Although the above approaches have demonstrated active tuning of topological states, most of them only focus on either TESs or TCSs. Only a few research reports have considered both the active adjustment and reconfiguration of TESs and TCSs in TPCs. Therefore, more flexible and effective methods for manipulating topological states and related devices are urgently required.

In recent years, the phase change material $Ge_2Sb_2Te_5$ (GST) has attracted significant interest because of its excellent tunability originating from the reversible and rapid phase transition speed and distinct permittivity difference between amorphous and crystalline phases [31]. GST can be rapidly switched between amorphous and crystalline phases on a nanosecond time scale using pulsed optical or electrical heating [32-33]. Its phase transition speed is faster than that of other phase change materials such as $BaTiO_3$, VO_2, and liquid crystals [34-35]. Compared with other optical and electrical tuning technologies [29,36], using the phase change of GST to manipulate electromagnetic waves is greener and more convenient. GST is an excellent candidate for tunable topological optical devices, and introducing GST into TPCs based on the VHE may result in a method for actively manipulating topological states. In this study, we propose a reconfigurable valley TPC based on the phase change material GST. The TPC enables active control of the operating frequency band and the propagation direction of TESs using the shift and shape change of the edge band. The active manipulation of TESs and TCSs in a triangular structure constructed using the TPC is simultaneously realized via GST phase transition. In addition, we also achieve a reconfigurable multichannel optical router that can dynamically establish optical channels and switch their on/off states. Our method of manipulating TESs and TCSs provides a novel strategy for designing reconfigurable topological photonic devices, such as photonic topological circuits, topological photonic switches, and optical couplers.

2　Structural design

Our proposed nanophotonic structure is configured with 2D PCs featuring a valley Hall-type topology. As shown in Fig. 1(a), the valley photonic structure comprises two honeycomb PCs (i.e., PC1 and PC2). Fig. 1(b) shows the details of the unit cells of PC1 and PC2. The unit cell of PC1 contains two nonequivalent hexagonal dielectric rods, i.e., the small rod $d_1=0.23a$ and the large rod $d_2=0.39a$, where a represents the lattice constant. Conversely, the sizes of the two hexagonal rods are altered to form another type of PC (i.e., PC2). Because PC2 is the inversion symmetry partner of PC1, they have the same band structure. Note that the irreducible parts of a honeycomb lattice with the same material and geometry exhibit equivalent effective permittivity, leading to C_6 point group

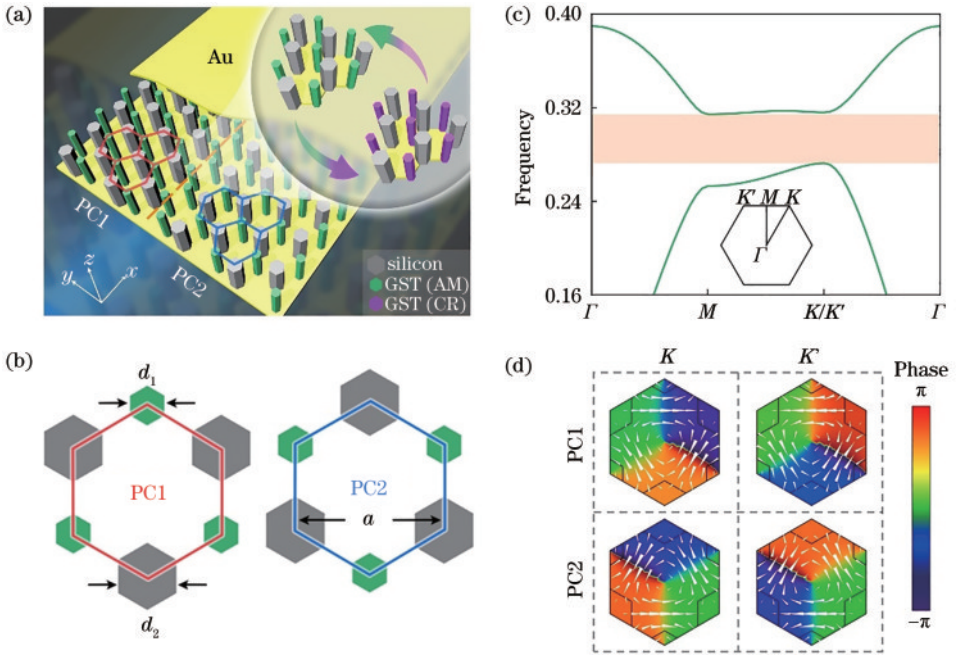

Fig. 1　Valley TPC structure and spectrum band. (a) Artistic illustration of switchable 2D topological PC consisting of hexagonal GST and Si rods; (b) schematic illustration of honeycomb lattice unit cells of PC1 and PC2. The gray and green rods represent Si and GST rods, respectively. d_1 and d_2 denote the distances between the opposite sides of small and large hexagonal rods, respectively; (c) band structure of TM mode for PC1/PC2 when GST is in an amorphous state. The inset shows the first Brillouin zone; (d) phase vortex of $\boldsymbol{E}_z$ at the K/K' valley for PC1 and PC2. The white arrows denote the power flow

symmetry. The spectrum band in the first Brillouin zone of the honeycomb lattice with C_6 is folded, forming doubly degenerate Dirac cones at K points. To split the Dirac point and induce a bandgap, the C_6 symmetry can be transformed into C_3 symmetry by replacing the material with a material with different permittivity or by adjusting the geometry parameters. For our nanophotonic structure, the inversion symmetry of PC1 and PC2 is broken, resulting in a full bandgap for the traverse magnetic (TM) mode, as shown in Fig. 1(c). In this study, we calculate the band structures of PCs and the intensity distributions and power flows of TESs using the COMSOL Multiphysics 6.0 software.

The electromagnetic field distribution in a PC characterizes its optical properties. Thus, it is necessary to analyze the field distribution of the eigenstate at the K/K' valley to discuss the topological phase in photonics based on the photonic VHE [37]. The maps of $\boldsymbol{E}_z$ and the average power flow at the K and K' valleys of the first band of PC1/PC2 are shown in Fig. 1(d). For the K valley, the phase of $\boldsymbol{E}_z$ in a unit cell of PC1 (PC2) decreases in the clockwise (counterclockwise) direction by a 2π phase around the unit cell center, and the direction of power flow as a vortex is the same as that of the decrease in the $\boldsymbol{E}_z$ phase. In contrast, for the K' valley, the direction of the decrease in the phase of $\boldsymbol{E}_z$ and the power flow in the unit cells of PC1 and PC2 are reversed. Such an optical vortex behaves as a spin-like binary DOF and can be termed a photonic valley DOF[11]. To demonstrate the topological phase in PCs, we calculated the Berry curvature distributions and valley Chern numbers. The details can be found in Appendix A. Because PC1 and PC2 have different valley Chern numbers (C_v), they have different topological phases. Specifically, because of the amorphous phase of GST, the C_v values of PC1 and PC2 are less and greater than zero, respectively.

3　Results and discussion

According to the bulk-edge correspondence [3], TESs exist in the bandgap of PCs when two different PCs are close to each other. To investigate the characteristics of TESs, we construct a supercell that holds an interface in the center formed by PC1 and PC2. We focus on two types of bearded interfaces (types A and B) and two types of bridge interfaces (types C and D) between PC1 and PC2. The details of the four types of interfaces can be found in Appendix B. Next, we consider the interface of type A shown in Fig. 2(a). The band structure of the supercell has an edge band inside the bandgap with an operation bandwidth of 0.2703–0.3142 c/a, as shown in Fig. 2(b).

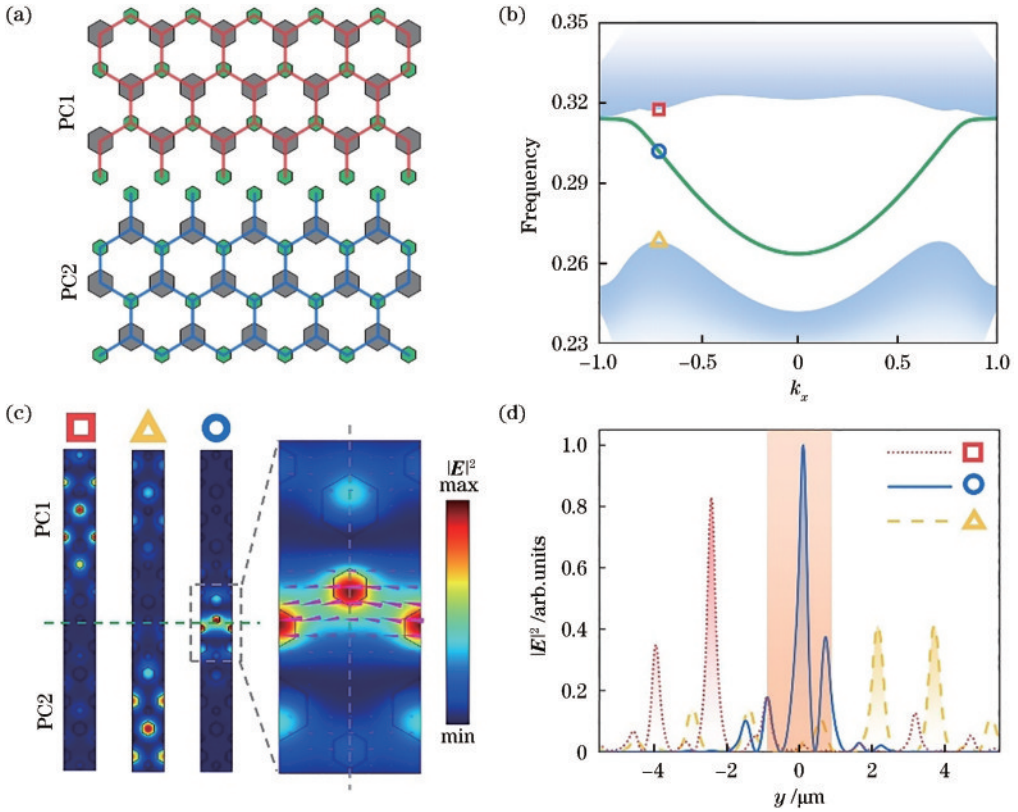

Fig. 2　TES in topological PCs. (a) Schematic of TPC constructed by PC1 and PC2 with a bearded interface (type A); (b) band structure of TPC when GST is in the amorphous phase. The blue region denotes the bulk band, and the green curve represents the edge band. The blue ring belongs to topological TES, and the red and yellow marks indicate bulk states located in the band spectrum; (c) $|\boldsymbol{E}|^2$ distributions of topological TES and bulk states. The pinkish red arrows in the enlarged figure represent the direction of power flow; (d) $|\boldsymbol{E}|^2$ distributions of topological TES and bulk states along the vertical midline (gray line) in Fig. 2(c). The yellow-shaded region marks the area around the interface with a width of two lattice constants

To check the intensity distribution of $|\boldsymbol{E}|^2$ in TPCs, we choose three points in the band structure with $k_x = -0.7\pi/a$, as shown in Fig. 2(b). One (blue ring) is located in the edge band, and the other two points (red and yellow rings) are located at the edges of the bulk spectrum. From Figs. 2(c) and 2(d), we observe that the electric fields of the in-gap edge states are primarily distributed near the interface between PC1 and PC2, whereas the electric fields of the bulk states are primarily localized in PC1 or PC2. The unidirectionality of the edge mode can be judged from the slopes (group velocities) of the edge band [38], as demonstrated by the power flow in Fig. 3(c). The U-shaped valley-dependent edge band exhibits a positive velocity at the K valley and a negative velocity at the K' valley; thus, the propagation directions of the edge modes at the K and K' valleys are opposite.

3.1　Propagation characteristics of TES on interface

Next, we investigate the propagation properties of TESs existing at straight and Z-shaped interfaces. A magnetic dipole source with $f = 0.2974\ c/a$ is located at the left end of the interfaces to excite TESs. In Fig. 3(a), the edge mode propagates along the straight interface with low loss, whereas it quickly attenuates in the vertical direction away from the interface. In particular, the edge mode can smoothly propagate around the two sharp corners of the Z-shaped interface, as shown in Fig. 3(b), suggesting that it can manipulate electromagnetic waves. Fig. 3(c) shows the simulated transmission spectra of the straight and Z-shaped interfaces. We observe that both spectrum curves exhibit a high-transmittance platform in the bandgap region, which indicates that the edge modes have good transmission performance. The robust transport of edge modes can be attributed to the suppression of intervalley scattering [37].

Unidirectional transport is an important property of valley-dependent TESs because it introduces a DOF for manipulating light. To reveal the chiral character of TESs, we place a chiral point source S_+ (S_-) at the center of the straight interface. The chiral point source S_+/S_- is expressed in terms of $H_0 e^{i\omega t}(\hat{\boldsymbol{x}} \mp \hat{\boldsymbol{y}})$, where H_0 denotes the amplitude, ω denotes the frequency, and $\hat{\boldsymbol{x}}$ and $\hat{\boldsymbol{y}}$ denote the unit vectors along the x and y directions, respectively. Figs. 3(d) and 3(e) show the intensity maps of $|\boldsymbol{E}|^2$ of TESs on the x-y plane for the chiral point

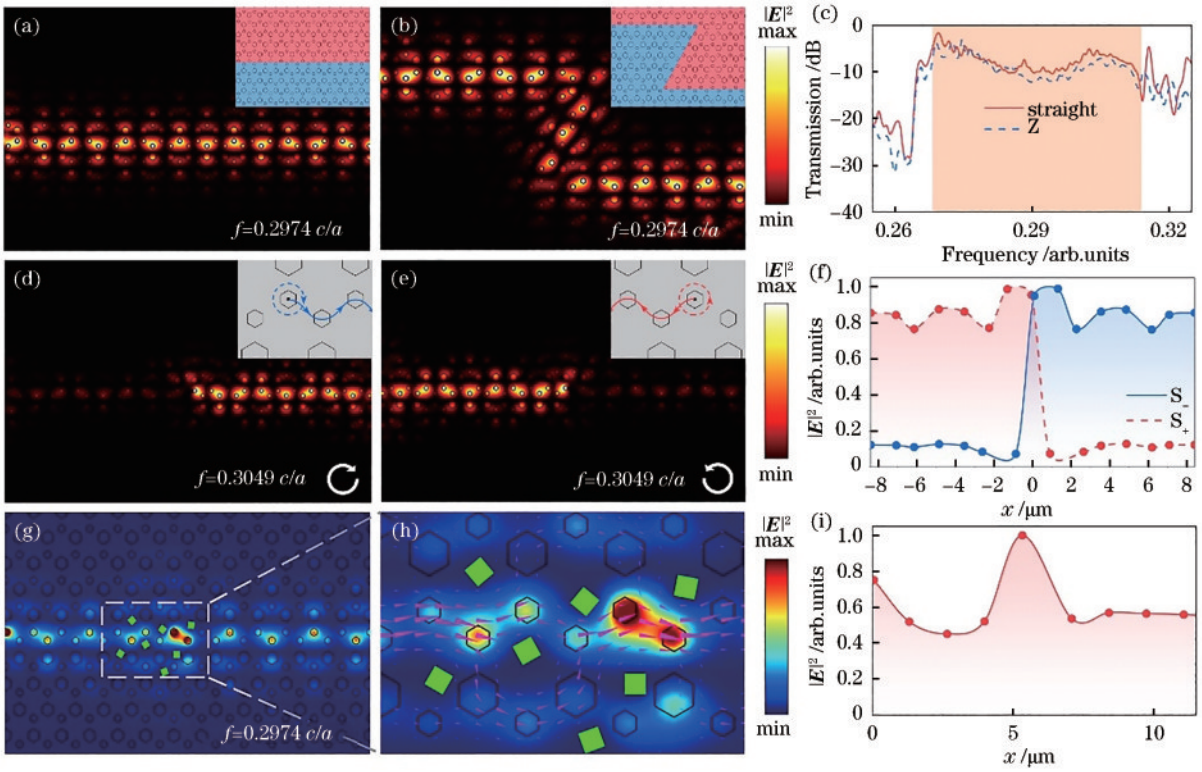

Fig. 3　Field maps of TESs and their transmission properties. (a) (b) Intensity maps of $|\boldsymbol{E}|^2$ of TES on the x-y plane for straight and Z-shaped interface structures. A magnetic dipole source with $f = 0.2974\ c/a$ is located at the left end of the interface; (c) transmission spectra of the straight and Z-shaped interface structures. The colored region denotes the bandgap of TPC; (d) (e) intensity maps of $|\boldsymbol{E}|^2$ for chiral point sources S_- and S_+ with $f = 0.3049\ c/a$. The light source is located at the center of the interface. The insets show a sketch of the unidirectional transport of TESs; (f) $|\boldsymbol{E}|^2$ distribution along the interfaces in Figs. 3(d) and 3(e). The data of $|\boldsymbol{E}|^2$ come from the maxima along the interfaces in Figs. 3(d) and 3(e), and then we interpolate many points to create smooth curves; (g) intensity map of $|\boldsymbol{E}|^2$ of TESs in the interface structure with defects of square gold rods. The side width of square gold rods is $0.2a$. A magnetic dipole source with $f = 0.2974\ c/a$ is located at the left end of the interface; (h) intensity map of $|\boldsymbol{E}|^2$ in the region of the sample denoted by the white dashed rectangle in Fig. 3(g). The green square gold rods denote defects, and the pinkish red arrows represent power flow; (i) $|\boldsymbol{E}|^2$ distribution along the interface in Fig. 3(g)

sources S_- and S_+, respectively. In the case of the S_- (S_+) source, the edge mode propagates only along the right (left) side interface, confirming that the designed valley-dependent topological interface can realize unidirectional propagation by controlling the chirality of the source. The intensity distributions of $|\boldsymbol{E}|^2$ along the interfaces shown in Figs. 3(d) and 3(e) are displayed in Fig. 3(f). For the S_- (S_+) source, the intensity of $|\boldsymbol{E}|^2$ at the right end of the interface is greater (less) than seven times that at the left end of the interface. In this structure, the intrinsic mechanism of unidirectional transport is that the optical vortex fields around bearded rods in the upper domain interact with those in the lower domain, thereby generating chiral transport edge modes [37].

Immunity to various defects is also a significant property of TESs. To verify this property, we placed several obstacles (square gold rods) as defects near a straight interface, as shown in Fig. 3(g). We found that the intensity distribution of $|\boldsymbol{E}|^2$ near the region with defects is slightly different from that in other regions because of the influence of the existence of defects on the propagation of electromagnetic waves. The edge mode can propagate from the left end of the interface to the right end and pass around obstacles without noticeable backscattering, indicating that TESs remain stable against defects. This property of extraordinary robustness has great application potential against manufacturing defects and environmental disturbances.

3.2　Reconfiguring topological edge states by phase change of GST

GST is a phase change material, and its amorphous and crystalline phases have distinctive permittivities. We note that the permittivities of amorphous or crystalline GST vary slightly in the wavelength region of 3–5 μm [39]; thus, it can be considered a constant in this wavelength range. In this study, the relative permittivities of amorphous and crystalline GST are 16.0 and 34.0, respectively, as shown in Fig. 4(a). The material

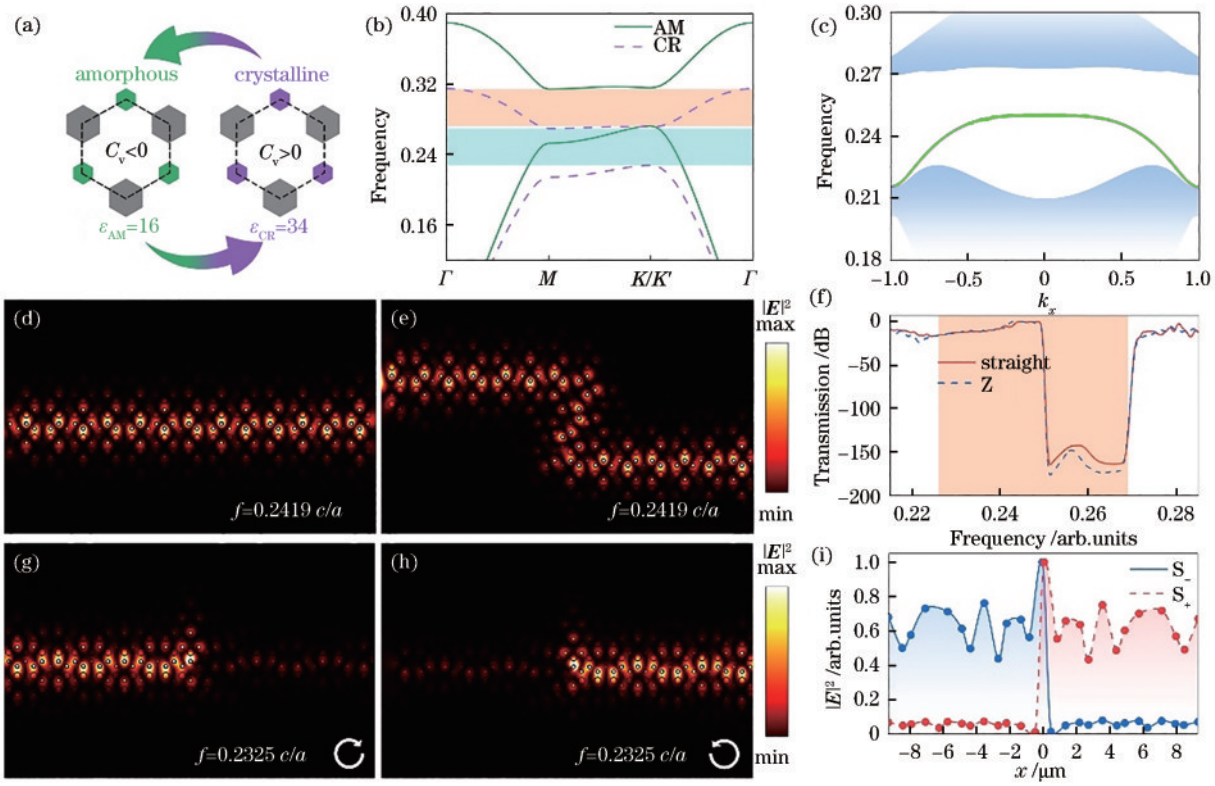

Fig. 4　TESs switched by the phase change of GST. (a) Schematic of unit cells with rods of phase change material GST. The relative permittivities of amorphous and crystalline GSTs are taken as 16 and 34, respectively; (b) band structures of PC1 (PC2) when GST is in amorphous and crystalline phases; (c) band structure of TPC [Fig. 2(a)] when GST is in crystalline phase. The blue regions denote bulk bands of TPC, and the green curve represents edge bands; (d) (e) intensity maps of $|\boldsymbol{E}|^2$ on the x-y plane for the straight and Z-shaped interface structures when GST is in the crystalline phase. A magnetic dipole source with $f=0.2419\ c/a$ is located at the left end of the interface; (f) transmission spectra of straight and Z-shaped interface structures. The colored region denotes the bandgap of TPC; (g) (h) intensity maps of $|\boldsymbol{E}|^2$ at $f=0.2325\ c/a$. A chiral point source S_-(S_+) is located at the center of the interface; (i) $|\boldsymbol{E}|^2$ distribution along the interface in Figs. 4(g) and 4(h). The data of $|\boldsymbol{E}|^2$ come from the maxima along the interface in Figs. 4(g) and 4(h), and we then interpolate many points to make a smooth curve

parameters of Si are obtained from Ref. [40]. We calculated the photonic band dispersion of PC1/PC2 for the crystalline phase of GST, as shown in Fig. 4(b). For comparison, Fig. 4(b) shows the photonic band dispersion of PC1/PC2 for the amorphous phase of GST. The numerical results show that the bandgap becomes narrow and is redshifted from 0.2703−0.3142 c/a to 0.2281−0.2694 c/a as GST transitions from the amorphous phase to the crystalline phase. Correspondingly, the operation bandwidth of TESs changes from 0.2703−0.3142 c/a [Fig. 2(b)] to 0.2281−0.2500 c/a [Fig. 2(c)]. The above phenomena indicate that the positions and widths of the bandgap and edge band of TPCs strongly depend on the material parameters of unit cells, and they can be actively adjusted using the phase change of GST. For the amorphous phase of GST, the effective permittivity near the area around the GST rods is smaller than that around the Si rods, whereas the former is larger than the latter in the case of the crystalline phase. The phase change of GST leads to symmetry inversion; thus, the topological phase of PCs is changed. To verify the above deduction, we calculated the valley Chern number of PCs (see Appendix A). The valley Chern number of PC1 (PC2) is less (larger) than zero for the amorphous phase, whereas the valley Chern number of PC1 (PC2) is larger (less) than zero for the crystalline phase. Therefore, the shape of the edge band of TPCs changes significantly, i.e., the edge band is inversed from a "∪" shape [Fig. 2(b)] to an "∩" shape [Fig. 4(c)] when GST transitions from the amorphous phase to the crystalline phase. The above reconfiguration method allows us to actively manipulate the topological phase of PCs by controlling the structural phase of GST.

Because there is no overlap between the operation bands of edge modes in the cases of amorphous and crystalline phases, TESs for the crystalline (amorphous) phase of GST are switched off when GST changes from the crystalline (amorphous) phase to the amorphous

(crystalline) phase, and vice versa. For example, a TES at $f = 0.2419\ c/a$ can propagate along the straight and Z-shaped interfaces of TPCs when GST is in the crystalline phase, as shown in Figs. 4(d) and 4(e). However, the electromagnetic mode at this frequency cannot propagate along straight or Z-shaped interfaces when GST changes from the crystalline phase to the amorphous phase. Similarly, the TESs at the interfaces for the crystalline phase of GST exhibit high transmittance, as shown in Fig. 4(f). The propagation direction of TESs can be directly judged from the slope of the TES in the topological edge band. According to the shapes of the edge bands of TPCs in amorphous and crystalline phases, for the same chiral source, the propagation direction of TESs in the amorphous phase is opposite to that in the crystalline phase. The intensity distributions of $|\boldsymbol{E}|^2$ in Figs. 4(g) and 4(h) validate the above analysis. At $f = 0.2325\ c/a$, the TES mode excited by S_- (S_+) propagates toward the left (right) side, and the propagation direction is opposite to that in Fig. 3(d) and 3(e).

3.3 Reconfiguring topological corner states by phase change of GST

Two different PCs with opposite topological phases generate TESs on the interface between them, and TCSs appear at the crossing of the two interfaces. In other words, 2D bulk topology yields 1D TESs, and the topology of gapped 1D TESs yields 0D TCSs, demonstrating the high-order topology [41]. Among the band structures of the interfaces of types A–D, only the band structures of the interfaces of types C and D have a gap between edge and bulk bands or between two edge bands when GST is in both amorphous and crystalline phases (Fig. 9), which may lead to the emergence of TCSs. To confirm this deduction, we constructed a triangular PC structure with the interface of type C [the inset in Fig. 5(a)], where the triangular PC1 region is surrounded by an outer triangular PC2 region. Detailed information about the corner states in the triangular PC structure with the interface of type D can be found in Appendix C. As shown in Fig. 5(a), there are three near-degenerated TCSs in the gap between two edge bands when GST is in the amorphous phase. The operating frequency of this group of TCSs is approximately $0.2947\ c/a$. According to the evaluation of the intensity distribution of $|\boldsymbol{E}|^2$, TCSs are strongly localized at three corners of the triangular PC structure, as shown in Fig. 5(c) I. To verify the existence of TCSs, we place a chiral point source S_+ at the center of the horizontal interface. The simulated result is shown in Fig. 5(c) II. The intensity distribution of $|\boldsymbol{E}|^2$ is consistent with that of the corner state at the

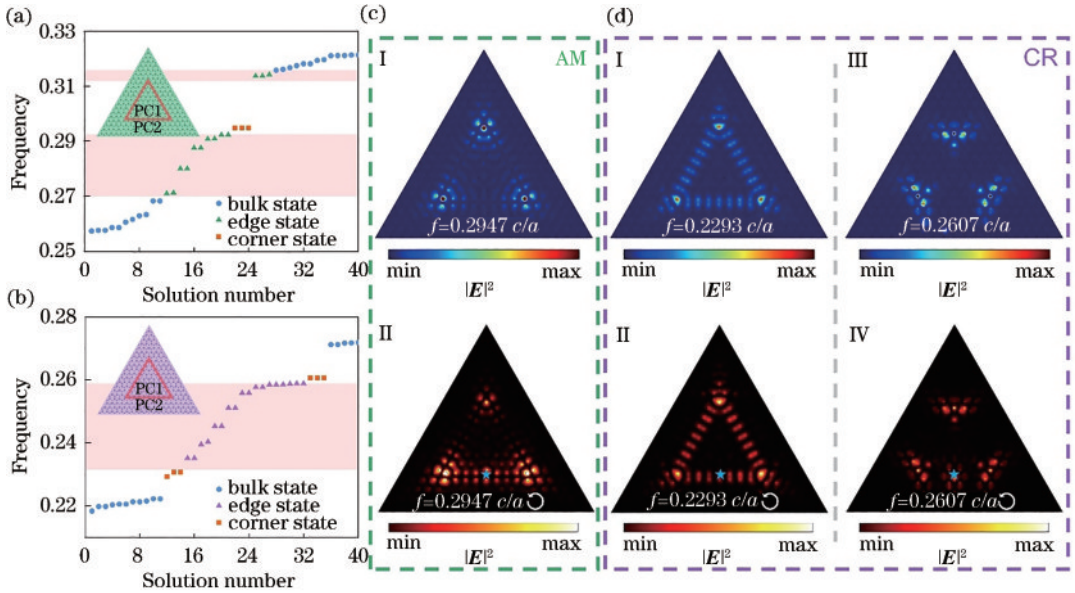

Fig. 5 TCSs in triangular PC structure with the interface of type C. (a) (b) Eigenfrequencies of the triangular PC structure when GST is in amorphous and crystalline phases. The blue, purple (green), and orange dots represent bulk, edge, and corner states, respectively, and the colored region indicates the range of edge bands. The inset shows a sketch of the triangular topological PC structure; (c) intensity map of $|\boldsymbol{E}|^2$ of the corner state at the eigenfrequency of $f = 0.2947\ c/a$ when GST is in amorphous phase (I), and intensity map of $|\boldsymbol{E}|^2$ of the corner state excited by chiral point source S_+ with $f = 0.2947\ c/a$ (II); (d) intensity maps of $|\boldsymbol{E}|^2$ of corner states at the eigenfrequencies of $f = 0.2293\ c/a$ (I) and $0.2607\ c/a$ (III) when GST is in crystalline phase, and intensity maps of $|\boldsymbol{E}|^2$ of the corner states excited by chiral point source S_+ with $f = 0.2293\ c/a$ (II) and $0.2607\ c/a$ (IV)

eigenfrequency in Fig. 5(c) I, showing that TCSs emerge near the corners of the triangular PC structure. Because transmission loss exists, the intensity of the TCS near the light source is larger than that far away from the light source. In addition, we found that the available bandwidth of TCSs is narrower than that of TESs, which indicates that TCSs are more sensitive to frequency than TESs.

When the structural phase of GST in the entire triangular structure is changed from amorphous to crystalline, two groups of TCSs appear in the gap between the bulk and edge bands, and each group has three near-degenerated TCSs, as shown in Fig. 5(b). One group is below the edge band with a low frequency, and the other near is above the edge band with a high frequency. To distinguish the two groups of TCSs, we named them low-frequency corner states (LFCSs) and high-frequency corner states (HFCSs), respectively. Their intensity distributions at eigenfrequencies are shown in Figs. 5(d) I and 5(d) III, respectively. When a chiral point source S_+ is placed on the horizontal interface, as shown in Figs. 5(d) II and 5(d) IV, TCSs are effectively excited. The HFCSs remain well-localized and are distinguishable from TES. In contrast, the operating frequencies of the LFCSs are close to the edge band; thus, the LFCSs are much less localized and become similar-looking edge states. The reason is that the HFCSs result from a bulk topology, whereas the LFCSs may have originated from long-range couplings between adjacent edge states [42]. The above phenomena suggest that the phase transition of GST in a triangular structure leads to a large frequency shift of TCSs, along with a change in the group number of TCSs, thereby achieving active reconfiguration of corner states. The reconfiguration of TCSs may facilitate the design of tunable corner topological devices, such as corner lasers. In addition to TCSs, the frequency interval of TESs in triangular PC structures exhibits a significant shift in the process of GST phase transition. This suggests that both topological edge and corner states can be simultaneously adjusted and reconfigured via GST phase transition.

3.4 Reconfigurable multichannel optical router

Based on the adjustability of the TESs of TPCs with GST, we designed a multichannel optical router, as shown in Fig. 6. In the central rhombus region, only one type of PC exists (i.e., PC1), and PC1 and PC2 are alternately distributed around the central rhombus region. Each side of the rhombus region has 15 units. Eight ports are distributed in four directions (up, down, left, right) in the router, with two ports in each direction. Two types of interfaces (i.e., types A and B) are formed in the router, and they have different edge bands with an overlapping operation bandwidth, allowing TESs to propagate from one type of interface to another. To ensure high coupling strength, all interfaces parallel to the side of the rhombus should be as close to each other as possible [27]. For our proposed router, we can dynamically establish a channel between any two adjacent ports by switching the structural phase of their nearby GST rods, and the availability of channels can be controlled by changing the structural phase of the GST rods in the central rhombus region. Here, we mainly discuss the four states of the two channels, which correspond to the two edge modes shown in Fig. 7(a) I–IV. As shown in Fig. 7(a) III, channels A and B are formed by the interfaces near ports 1 and 2 and ports 3 and 4, respectively. By changing the structural phase of the GST rods in the central rhombus region, the two channels can be switched between "off" and "on". Therefore, there are four states for channels A and B. Specifically, when the GST rods in the central region are in the amorphous (crystalline) phase, channels A and B are in "on" ("off") and "off" ("on") states, respectively, as shown in Figs. 7(a) I and II. When the GST rods in the upper-right and lower-left parts of the center region are in crystalline and amorphous phases, respectively, channels A and B are in an "off" state, as shown in Fig. 7(a) III. As the GST rods in the upper-left and

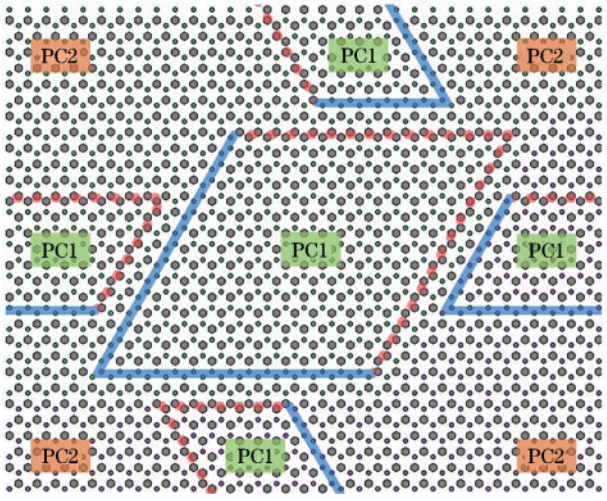

Fig. 6　Sketch of reconfigurable multichannel optical router. The large and small hexagons denote silicon and GST rods, respectively. The blue and red lines represent the topological interfaces of types A and B, respectively

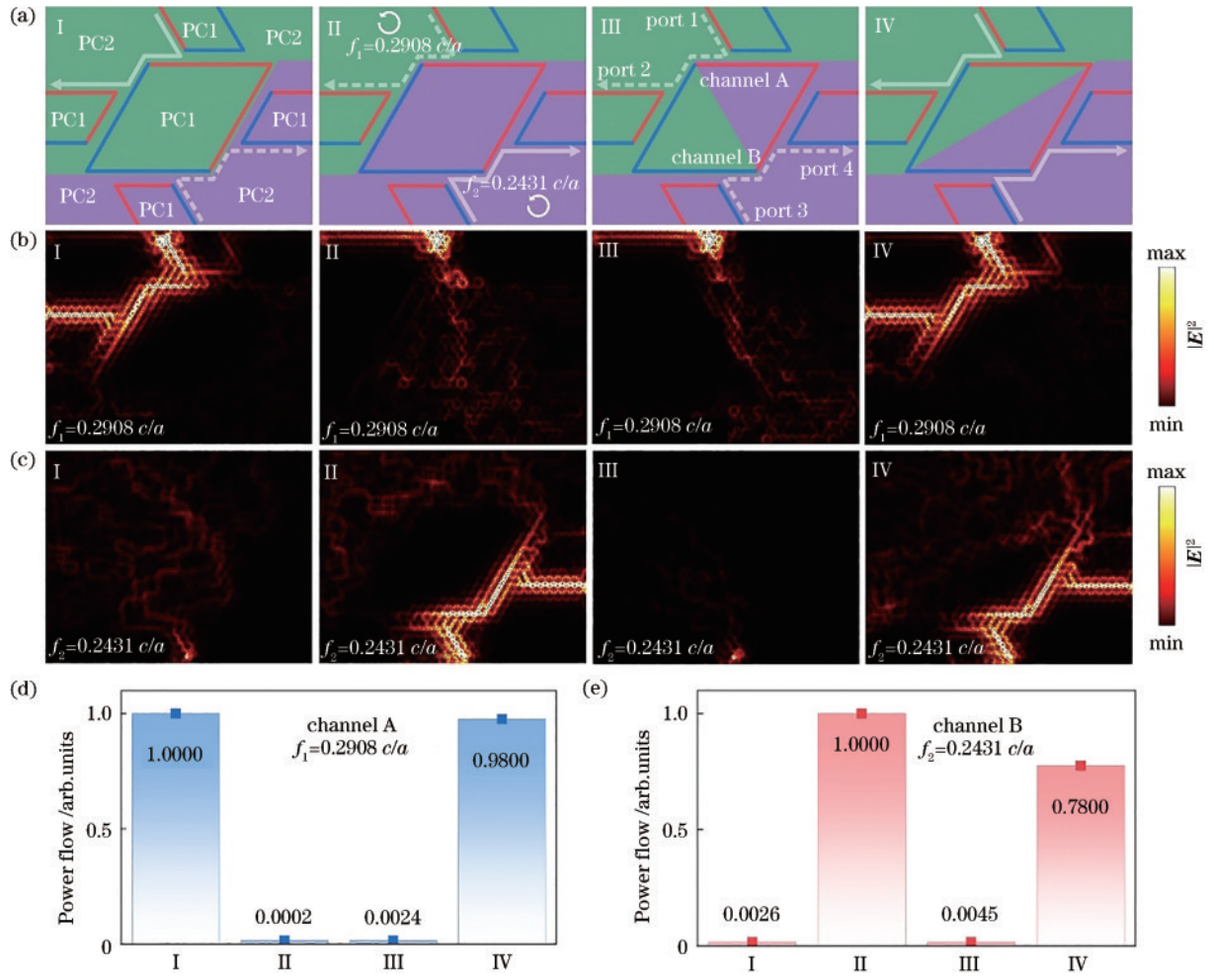

Fig. 7　Reconfigurable multichannel optical router based on TPCs with GST. (a) Sketches of our designed optical router. I–IV correspond to four different states of channels A (from port 1 to port 2) and B (from port 3 to port 4), respectively, i. e., the states of on-off (I), off-on (II), off-off (III), and on-on (IV). The green and purple regions denote PCs in which GST rods are in amorphous and crystalline phases, respectively. The white solid and dashed lines with arrows represent the "on" and "off" states of channels, respectively. The blue and red lines denote the interfaces of types A and B, respectively; (b) (c) maps of the power flow of four states of channels A and B. The operation frequencies of channels A and B are 0.2908 c/a (f_1) and 0.2431 c/a (f_2), respectively. A chiral point source S_+ for the excitation of TESs is set at ports 1 and 3; (d) (e) values of power flow at the outputs of channels A and B (i. e., ports 2 and 4) for four states

lower-right parts of the center region are in amorphous and crystalline phases, respectively, channels A and B are in "on" states, as shown in Fig. 7(a) IV.

According to the band structure of TPCs, we choose two operation frequencies, i. e., $f_1 = 0.2908\ c/a$ for channel A and $f_2 = 0.2431\ c/a$ for channel B. To evaluate the switching performance of channels A and B, we simulated the power flow of the four states of channels A and B, as shown in Figs. 7(b) and (c), respectively. From the maps of the power flow, we can observe the switching effect via the phase change of GST. For the case in Fig. 7(b) I, the signal with a frequency of 0.2908 c/a inputted from port 1 propagates along the straight interface and is then coupled into the upper border of the rhombus. Although there are two types of interfaces (i. e., types A and B) near the upper-left corner of the rhombus, the signal can pass around the corner, suggesting strong electromagnetic coupling between the two types of bearded interfaces. Finally, the signal is coupled into the left straight interface and is outputted from port 2. The above signal propagation indicates that channel A is in an "on" state. However, the signal with a frequency of 0.2431 c/a cannot propagate in channel B, as shown in Fig. 7(c) I. The reason for this is explained as follows. When the signal from port 3 is coupled into the border of the rhombus, its energy is quickly lost to the central rhombus region because the structural phases of the GST rods on the two sides of the interface near the lower-right corner of the rhombus region are different, and there is no overlap between the operation bands of edge modes for the interfaces on

channel B. The other three states in Figs. 7(a) II-IV and 7(b) II-IV can be analyzed using a similar method.

The power flow values at ports 2 and 4 in the above four states are shown in Figs. 7(d) and 7(e), respectively. We also calculated the on-off ratio of channels A and B, which is defined as the ratio of power at the output in the "on" state to that in the "off" state. When channel B is in an "off" ("on") state, the on-off ratio of channel A is 416.67 (4900.00). Conversely, when channel A is in an "off" ("on") state, the on-off ratio of channel B is 222.22 (300.00). The on-off ratio of one channel is associated with the "on" and "off" states of the other channel. To explain this phenomenon, we take the on-off ratio of channel A as an example. Figs. 7(a) I and 7(a) IV show the "on" state of channel A. Figs. 7(a) II and 7(a) III show the "off" state of channel A. The structural phase of GST near channel A in Fig. 7(a) I is the same as that in Fig. 7(a) IV. Thus, there is almost no difference in the distribution of the power flow. Conversely, the structural phase of GST near channel A in Fig. 7(a) II is different from that in Fig. 7(a) III. Comparing Figs. 7(a) II and 7(a) III, we find that the energy in the former enters into the central rhombus region and is lost more severely in this region than in the latter, resulting in less power at the outlet (i.e., port 2) in the former. Based on the above analysis, it is not difficult to understand that the on-off ratio of channel A when channel B is in an "off" state is smaller than that when channel B is in an "on" state. In addition, we placed several obstacles (square gold rods with a side width of $0.2a$) as defects near the channels (not shown here) and calculated the on-off ratios of channels A and B. We found that the on-off ratios of the channels differ slightly, which suggests that our router exhibits a good robustness. Notably, in addition to the above-mentioned channels, our router can reconfigure channels by adjusting the structural phase of GST around the central rhombus region (see Appendix D for more details).

Because of the ultra-fast speed of the phase transition of GST[32], the reconfiguration of our router can be completed in a very short time, which is advantageous for practical applications. Meanwhile, the propagation direction of TESs depends on the chirality of the excitation sources. Therefore, our reconfigurable router can tune the channels not only with high DOF but also at considerable speed. In addition, the permittivity of GST can be continuously tuned over a small range by controlling the annealing process[25], and such a feature can be applied to our TPC structures, which leads to a continuous tunable photonic router. This means that the operating bandwidth of TESs and TCSs in TPCs based on GST material can be continuously and dynamically tuned.

4 Conclusion

In summary, we successfully achieved the active reconfiguration of valley TESs and TCSs based on TPCs with the phase change material GST. TPCs comprise two inverse honeycomb PCs that consist of hexagonal silicon and GST rods. Because of the lack of in-valley coupling, valley-dependent TESs exhibit impressive robustness and efficient transport, which are important for light-field control and low-loss light device design. As GST transitions from the amorphous phase to the crystalline phase, the bandgap and edge band of TPCs exhibit a significant redshift. In addition, the valley topological phase of PCs is inversed, causing the edge band to change from "∪" to "∩" shape curves. Furthermore, we achieved active reconfiguration of TESs and TCSs in a triangular PC structure. The group number of corner states changes with the phase change of GST. Based on the adjustability of TESs and electromagnetic coupling between two different topological bearded interfaces, we designed a multichannel reconfigurable optical router that can dynamically reconfigure optical channels and switch their on/off states. This study paves a new way to explore the active and dynamical tuning of valley TESs and TCSs. Our findings will be crucial for the development of reconfigurable topological photonic devices.

References

[1] Jiang P, Ma N, Qiao X Z, et al. Recent progress in chiral topological quantum interface[J]. Frontiers in Physics, 2022, 10: 845579.

[2] Xue H R, Yang Y H, Zhang B L. Topological valley photonics: physics and device applications[J]. Advanced Photonics Research, 2021, 2(8): 2100013.

[3] Ozawa T, Price H M, Amo A, et al. Topological photonics[J]. Reviews of Modern Physics, 2019, 91(1): 015006.

[4] Wang Z, Chong Y D, Joannopoulos J D, et al. Observation of unidirectional backscattering-immune topological electromagnetic states[J]. Nature, 2009, 461(7265): 772-775.

[5] Poo Y, Wu R X, Lin Z F, et al. Experimental realization of self-guiding unidirectional electromagnetic edge states [J]. Physical Review Letters, 2011, 106(9): 093903.

[6] Cheng X J, Jouvaud C, Ni X, et al. Robust reconfigurable electromagnetic pathways within a photonic topological insulator[J]. Nature Materials, 2016, 15(5): 542-548.
[7] Tzuang L D, Fang K J, Nussenzveig P, et al. Non-reciprocal phase shift induced by an effective magnetic flux for light[J]. Nature Photonics, 2014, 8(9): 701-705.
[8] Fang K J, Yu Z F, Fan S H. Realizing effective magnetic field for photons by controlling the phase of dynamic modulation[J]. Nature Photonics, 2012, 6(11): 782-787.
[9] Wu L H, Hu X. Scheme for achieving a topological photonic crystal by using dielectric material[J]. Physical Review Letters, 2015, 114(22): 223901.
[10] Yang Y T, Qian X Y, Shi L W, et al. Observation and control of pseudospin switching in a finite-width topological photonic crystal[J]. Optics Express, 2022, 30(4): 5731-5738.
[11] Ma T, Shvets G. All-Si valley-Hall photonic topological insulator[J]. New Journal of Physics, 2016, 18(2): 025012.
[12] Yang Y H, Yamagami Y, Yu X B, et al. Terahertz topological photonics for on-chip communication[J]. Nature Photonics, 2020, 14(7): 446-451.
[13] Chen X D, Deng W M, Shi F L, et al. Direct observation of corner states in second-order topological photonic crystal slabs[J]. Physical Review Letters, 2019, 122(23): 233902.
[14] Xie B Y, Su G X, Wang H F, et al. Higher-order quantum spin Hall effect in a photonic crystal[J]. Nature Communications, 2020, 11: 3768.
[15] Zhang W X, Yuan H, Sun N, et al. Observation of novel topological states in hyperbolic lattices[J]. Nature Communications, 2022, 13: 2937.
[16] Liu Z R, Hua C B, Peng T, et al. Higher-order topological insulators in hyperbolic lattices[J]. Physical Review B, 2023, 107(12): 125302.
[17] Zhou R, Lin H, Wu Y J, et al. Higher-order valley vortices enabled by synchronized rotation in a photonic crystal[J]. Photonics Research, 2022, 10(5): 1244-1254.
[18] Tang G J, He X T, Shi F L, et al. Topological photonic crystals: physics, designs, and applications[J]. Laser & Photonics Reviews, 2022, 16(4): 2100300.
[19] Joannopoulos J D, Johnson S G, Winn J N, et al. Photonic crystals molding the flow of light[M]. Princeton: Princeton University Press, 2008.
[20] Kumar A, Gupta M, Pitchappa P, et al. Active ultrahigh-Q (0.2×10^6) THz topological cavities on a chip[J]. Advanced Materials, 2022, 34(27): 2202370.
[21] Ota Y, Liu F, Katsumi R, et al. Photonic crystal nanocavity based on a topological corner state[J]. Optica, 2019, 6(6): 786-789.
[22] Kim H R, Hwang M S, Smirnova D, et al. Multipolar lasing modes from topological corner states[J]. Nature Communications, 2020, 11: 5758.
[23] Kumar A, Gupta M, Pitchappa P, et al. Phototunable chip-scale topological photonics: 160 Gbps waveguide and demultiplexer for THz 6G communication[J]. Nature Communications, 2022, 13: 5404.
[24] Kang L J, Fei H M, Lin H, et al. Thermal tunable silicon valley photonic crystal ring resonators at the telecommunication wavelength[J]. Optics Express, 2023, 31(2): 2807-2815.
[25] Cao T, Fang L H, Cao Y, et al. Dynamically reconfigurable topological edge state in phase change photonic crystals[J]. Science Bulletin, 2019, 64(12): 814-822.
[26] Wu Y, Hu X Y, Gong Q H. Reconfigurable topological states in valley photonic crystals[J]. Physical Review Materials, 2018, 2(12): 122201.
[27] Mehrabad M J, Foster A P, Martin N J, et al. Chiral topological add-drop filter for integrated quantum photonic circuits[J]. Optica, 2023, 10(3): 415-421.
[28] Liu X D, Huang J L, Chen H, et al. Terahertz topological photonic waveguide switch for on-chip communication[J]. Photonics Research, 2022, 10(4): 1090-1096.
[29] Zhao Y L, Liang F, Han J F, et al. Tunable topological edge and corner states in an all-dielectric photonic crystal[J]. Optics Express, 2022, 30(22): 40515-40530.
[30] Shalaev M I, Desnavi S, Walasik W, et al. Reconfigurable topological photonic crystal[J]. New Journal of Physics, 2018, 20(2): 023040.
[31] Li P N, Yang X S, Maß T W W, et al. Reversible optical switching of highly confined phonon-polaritons with an ultrathin phase-change material[J]. Nature Materials, 2016, 15(8): 870-875.
[32] Rudé M, Mkhitaryan V, Cetin A E, et al. Ultrafast and broadband tuning of resonant optical nanostructures using phase-change materials[J]. Advanced Optical Materials, 2016, 4(7): 1060-1066.
[33] Hosseini P, Wright C D, Bhaskaran H. An optoelectronic framework enabled by low-dimensional phase-change films[J]. Nature, 2014, 511(7508): 206-211.
[34] Xiong C, Pernice W H P, Ngai J H, et al. Active silicon integrated nanophotonics: ferroelectric $BaTiO_3$ devices[J]. Nano Letters, 2014, 14(3): 1419-1425.
[35] Ko J H, Yoo Y J, Lee Y B, et al. A review of tunable photonics: optically active materials and applications from visible to terahertz[J]. iScience, 2022, 25(8): 104727.
[36] Shalaev M I, Walasik W, Litchinitser N M. Optically tunable topological photonic crystal[J]. Optica, 2019, 6(7): 839-844.
[37] He X T, Liang E T, Yuan J J, et al. A silicon-on-insulator slab for topological valley transport[J]. Nature Communications, 2019, 10(1): 872.
[38] Lu L, Joannopoulos J D, Soljačić M. Topological photonics[J]. Nature Photonics, 2014, 8(11): 821-829.
[39] Cao T, Bao J X, Mao L B, et al. Controlling lateral Fano interference optical force with Au-$Ge_2Sb_2Te_5$ hybrid nanostructure[J]. ACS Photonics, 2016, 3(10): 1934-1942.
[40] Li H H. Refractive index of silicon and germanium and its wavelength and temperature derivatives[J]. Journal of Physical and Chemical Reference Data, 1980, 9(3): 561-658.
[41] Zhang Y X, Li Z F, Xu S X, et al. Tunable and reconfigurable higher-order topological insulators in photonic crystals with phase change materials[J]. Annalen Der Physik, 2022, 534(1): 2100293.

[42] Wang H X, Liang L, Jiang B, et al. Higher-order topological phases in tunable C_3 symmetric photonic crystals[J]. Photonics Research, 2021, 9(9): 1854-1864.

Appendix A: Characterization of topology: Berry curvature and valley Chern number

To characterize the topological phase of PCs, we calculated the Berry curvature and valley Chern number of PCs' first band by the opened source software MPB. As shown in Fig. 8, for either amorphous or crystalline phase of GST, the Berry curvatures of PC1 (PC2) at the K and K' points are equal and opposite. The valley-dependent Chern number is calculated by

$$C_{K/K'}=\frac{1}{2\pi}\int_{HBZ_{k/k'}}\Omega(k)\mathrm{d}^2k\,, \tag{1}$$

where $\Omega(k)$ is Berry curvature. The valley Chern number (C_v) is the difference between the valley-dependent Chern number of K and K' valley, i. e., $C_v=C_K-C_{K'}$. In the case of amorphous (crystalline) phase, the valley Chern numbers of PC1 (PC2) and PC2 (PC1) are less and larger than zero, respectively. For the same structural phase, the C_v of PC1 is opposite to that of PC2. When GST is changed from amorphous phase to crystalline phase, the valley Chern number of PC1 (PC2) is changed from a negative (positive) number to a positive (negative) number, and its absolute value has a slight change.

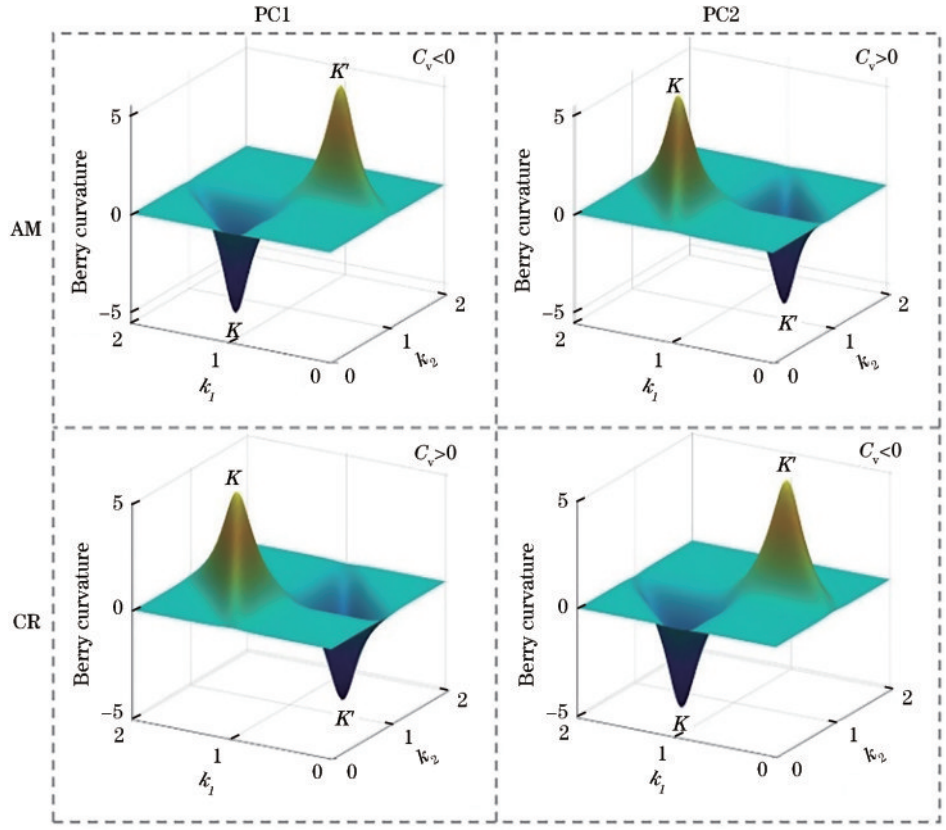

Fig. 8　Berry curvature distributions of the first band and valley Chern numbers of PC1 and PC2 in amorphous (AM) and crystalline (CR) phases

Appendix B: Topological interfaces of types A-D

Two types of bearded interfaces (i. e., types A and B) and two types of bridge interfaces (i. e., types C and D) are shown in Fig. 9(a). For the bearded interfaces, PC1 and PC2 are misaligned by half a unit, characterized by the proximity of either GST rods (type A) or Si rods (type B). With respect to the bridge interfaces, two PCs are aligned to each other, characterized by the proximity of either Si rods (type C) or GST rods (type D). Since all four types of interfaces are constructed by PC1 and PC2, their bulk band structures and gaps of TPCs are the same. The edge bands for four types of interfaces in the amorphous and crystalline phases are illustrated in Figs. 9(b) and 9(c), respectively. When the GST rods in TPC are in amorphous phase in Fig. 9(b), the edge bands of four types of interfaces are 0.2703 c/a-0.3142 c/a (type A), 0.2703 c/a-0.3000 c/a (type B), 0.2703 c/a-

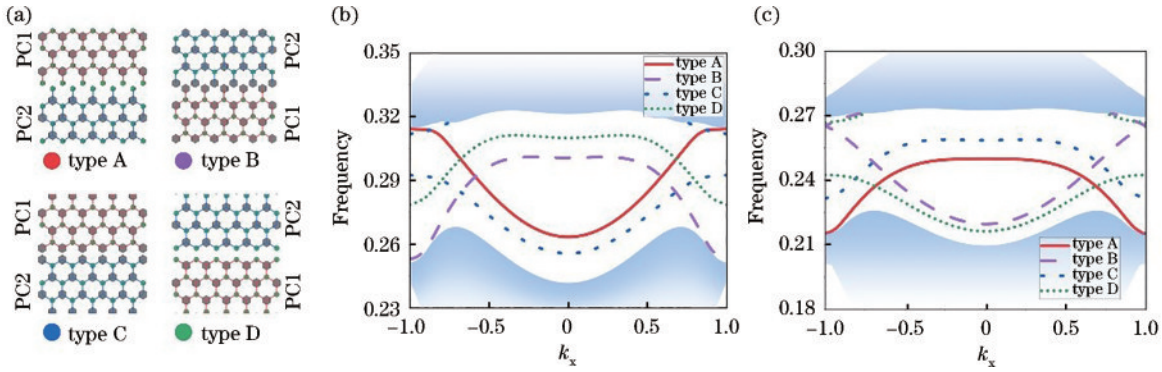

Fig. 9 Topological interfaces of types A-D and edge bands of TPC. (a) Schematics of TPCs with the interfaces of types A, B, C, and D; (b) (c) band structures of TPCs when GST is in amorphous and crystalline phases. The red, purple, blue, and green curves correspond to the topological interfaces of types A, B, C and D, respectively

0.2925 c/a (type C), and 0.2787 c/a-0.3112 c/a (type D) respectively. Due to the inversion of PCs at two sides of interface, the edge band of the interface of type A (C) exhibits the shape of "∪", while the edge band of the interface of type B (D) is the shape of "∩". When the structural phase of GST is changed into crystalline phase in Fig. 9(c), the edge bands of four types of interfaces shift to the interval of 0.2281 c/a-0.2500 c/a (type A), 0.2281 c/a-0.2703 c/a (type B), 0.2316 c/a-0.2589 c/a (type C) and 0.2281 c/a-0.2425 c/a (type D), respectively, and their shapes are almost upside down. The Overlapping area between operating bandwidth of TESs in two types of interfaces allows the light transport from one interface to another.

Appendix C: Reconfiguration of topological corner states in triangular PC structure with the interface of type D

In the main text, we have demonstrated the reconfiguration of topological corner states (TCSs) in triangular PC structure with the interface of type C. Here we construct a triangular PC structure with the interface of type D, the other geometrical parameters are the same as those in the case of type C. As displayed in Fig. 10(a), there are two groups of

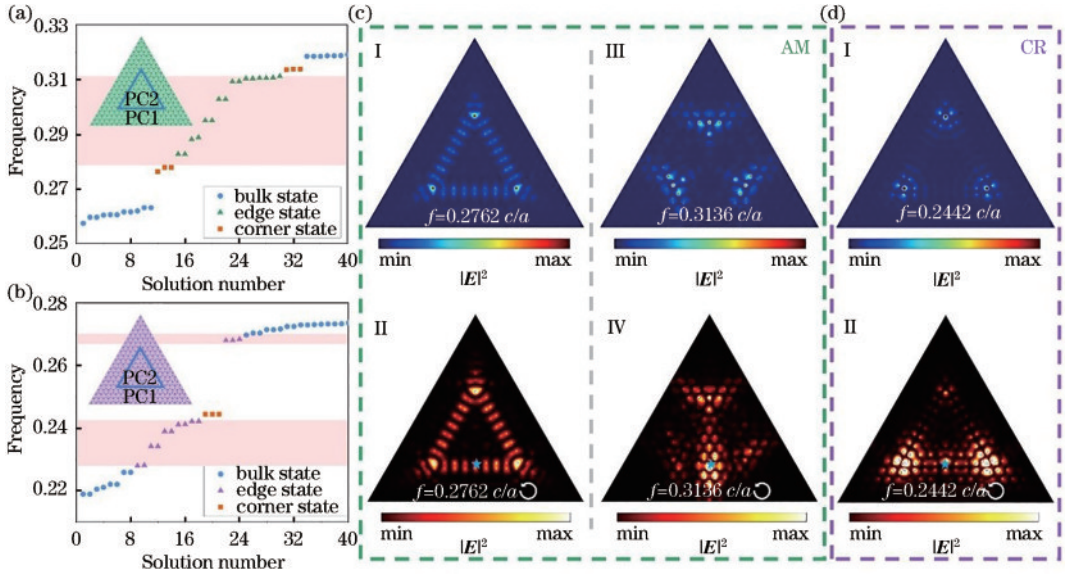

Fig. 10 TCSs in triangular PC structure with the interface of type D. Eigenfrequencies of the triangular PC structure as GST is in amorphous (a) and crystalline (b) phases. The blue, purple (green), and orange dots represent bulk state, edge state, and corner state, respectively, and the colored regions denote the range of edge bands. The inserts show the sketch of triangular topological PC structure; (c) intensity distributions of $|\boldsymbol{E}|^2$ of two groups of corner states at the eigenfrequencies of f=0.2762 c/a (I) and 0.3136 c/a (III) as GST is in crystalline phase, and intensity distributions of $|\boldsymbol{E}|^2$ of the corner states excited by chiral point source S_+ with f=0.2762 c/a (II) and 0.3136 c/a (IV); (d) intensity distribution of $|\boldsymbol{E}|^2$ of the corner state at the eigenfrequency of f=0.2442 c/a as GST is in amorphous phase (I), and intensity distribution of $|\boldsymbol{E}|^2$ of the corner state excited by chiral point source S_+ with f=0.2442 c/a (II)

neared-degenerated TCSs in the gaps between bulk band and edge band when GST is in amorphous phase. The groups of low-frequency corner states (LFCSs) and high-frequency corner states (HFCSs) are near 0.2762 c/a and 0.3136 c/a, respectively. The intensity distributions of $|\boldsymbol{E}|^2$ indicate that the TCSs are localized at the corners of triangular structure, as shown in Fig. 10(c) I and III. Because the frequencies of LFCSs are close to the operating bandwidth of TESs, the LFCSs are much less localized and become similar-looking edge states. As a chiral point source is placed on the horizontal interface, the LFCS and HFCS can be effectively excited, as shown in Figs. 10(c) II and 10(c) IV, respectively. Because the quality factor of triangular structure at the frequency of 0.3136 c/a is rather small, the intensity of $|\boldsymbol{E}|^2$ at the left and right corners is not obvious enough, as shown in Fig. 10(c) IV. When the GST changes from amorphous to crystalline phase shown in Fig. 10(b), the TCSs have a large redshift, and there is only one group of TCSs in the gap between bulk band and edge band. The intensity distribution of $|\boldsymbol{E}|^2$ at the eigenfrequency $f=0.2442\ c/a$ is displayed in Fig. 10(d) I, and the corresponding intensity distribution of TCS excited by chiral point source S_+ is shown in Fig. 10(d) II. The intensity distributions in the two figures are consistent with each other.

Appendix D: Reconfiguring the channels of optical router

In the main text, we have demonstrated the "on" and "off" states of the two channels in optical router where the channels A and B are situated at the top-left and lower-right corners, respectively. By tuning the structural phase of GST, channels A and B can be rebuilt at the top-right corner (channel A) and the

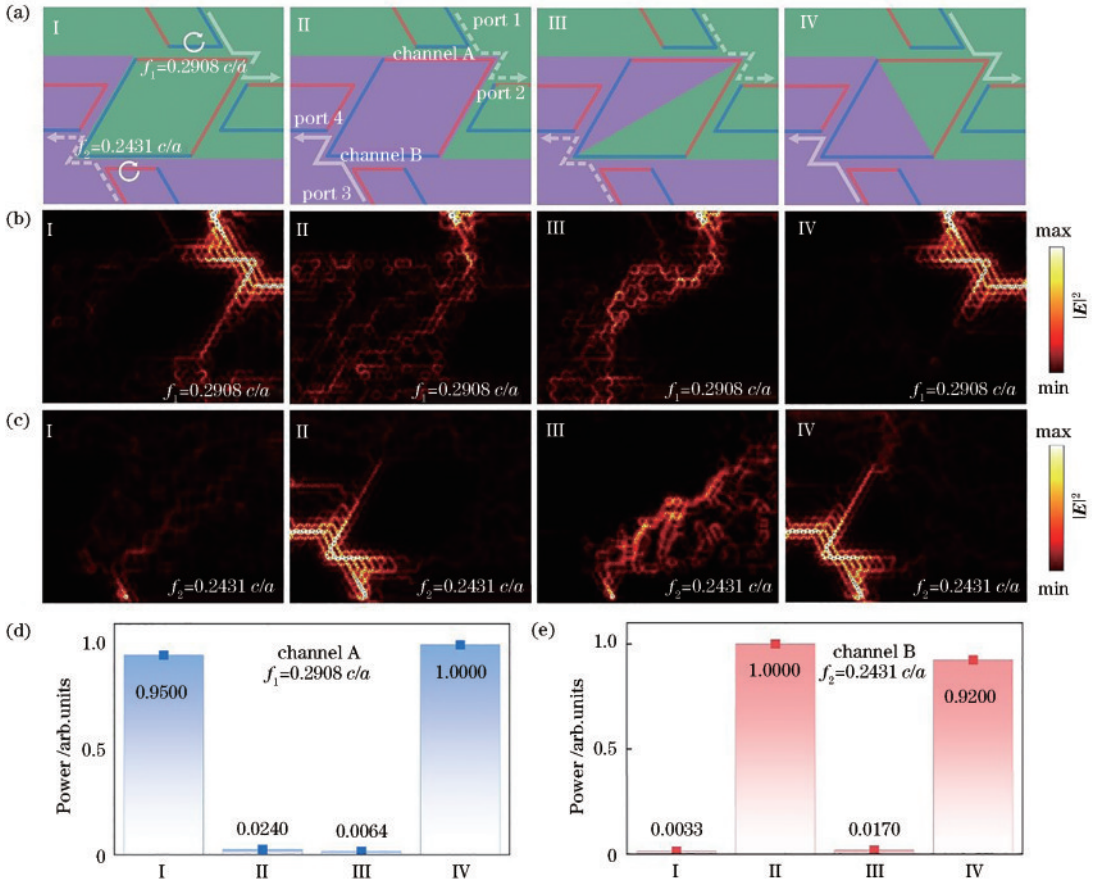

Fig. 11 Reconfigurable multichannel optical router based on the topological PCs with phase change material GST. (a) Sketches of our designed optical router. I-IV correspond to four states of channels A (from port 1 to port 2) and B (from port 3 to port 4), respectively, i.e., the states of on-off (I), off-on (II), off-off (III) and on-on (IV). The green and purple regions denote PC where GST rods are in amorphous and crystalline phases, respectively. The white solid and dashed lines with arrows represent the "on" and "off" states of channels, respectively. The blue and red lines denote the interfaces of types A and B, respectively. (b) (c) maps of power flow of four states of channels A and B. The operation frequencies of channels A and B are $f_1=0.2908c/a$ and $f_2=0.2431c/a$, respectively. A chiral point source for the excitation of TESs is set at ports 1 and 3; (d) (e) values of power flow at the outputs of channels A and B (i.e., ports 2 and 4) for four states

down-left corner (channel B), respectively, as shown in Fig. 11. Similarly, there exist four states for channels A and B. Specifically, when the GST rods in central region are in amorphous phase, the channels A and B are in "on" and "off" states, respectively in Fig. 11(a) I. As the GST rods in central region are in crystalline phase, channels A and B are switched into "off" and "on" states, respectively in Fig. 11(a) II. As the GST rods in the upper-left and lower-right parts of center region are in crystalline and amorphous phases, respectively, both channels A and B are switched into "off" state shown in Fig. 11(a) III. When the GST rods in upper-right and lower-left parts of center region are in amorphous and crystalline phases, respectively, both channels A and B are switched into "on" states in Fig. 11(a) IV. The maps of power flow in Figs. 11(a) and 11(b) confirm the four states of channels A and B. The power values at outputs (i. e., ports 2 and 4) in the above four states are illustrated in Figs. 11(d) and 11(e), respectively. When channel B is in "off" ("on") state, the on-off ratio of channel A is 148.44 (41.67). Conversely, when channel A is in "off" ("on") state, the on-off ratio of channel B is 58.82 (278.79). It should be pointed out that the chirality of point source and distributions of amorphous and crystalline GST rods around the central rhombus region in Figs. 11(a) are different from those in Fig. 7(a) in the main text. For the state of off-off, we find that the power flows in Fig. 11(b) III and Fig. 11(c) III are very different from those in Fig. 7(b) III and Fig. 7(c) III in main text, the distribution ranges of the power flows in the former are larger than those in the latter. The main reasons are as follows. First, the channels A and B in the former are located at top-right corner and down-left corner, respectively, while the channels A and B in the latter are located at top-left corner and down-right corner, respectively. Second, the routes of the channels A and B in the former are different from those in the latter. Third, there are differences in the distributions of interfaces of type A and type B and amorphous and crystalline GST rods on channels. Different distributions of interfaces and GST rods lead to different distributions of power flows.